Supporting Information Appendix for

An Ultrathin Dendrimer-Graphene Oxide Composite Film for Stable Cycling Lithium-Sulfur Batteries

Wen Liu[1,ǂ], Jianbing Jiang[1,ǂ], Ke R. Yang[1,ǂ], Yingying Mi[1,2,ǂ], Piranavan Kumaravadivel[1,3], Yiren Zhong[1], Qi Fan[1,4], Zhe Weng[1], Zishan Wu[1], Judy J. Cha[1,3,5], Henghui Zhou[2], Victor S. Batista[*,1], Gary W. Brudvig[*,1], Hailiang Wang[*,1]

[1]Department of Chemistry and Energy Sciences Institute, Yale University, 810 West Campus Drive, West Haven, CT 06516, USA

[2]College of Chemistry and Molecular Engineering, Peking University, Beijing 100871, China

[3]Department of Mechanical Engineering and Materials Science, Yale University, 15 Prospect Street, New Haven, CT 06511, USA

[4]Current address: school of Chemistry and Chemical Engineering, Southeast University, Nanjing, Jiangsu 211189, China

[5]Center for Research on Interface Structures and Phenomena, Yale University, 15 Prospect Street, New Haven, CT 06511, USA

[ǂ]These authors contributed equally

[*]E-mail: hailiang.wang@yale.edu; gary.brudvig@yale.edu; victor.batista@yale.edu

MATERIALS AND METHODS

Synthesis of Naph-Den and preparation of Naph-Den-mGO slurry

All chemicals and solvents were commercially available and used as obtained without further purification. Following a reported procedure (1) with modifications, a mixture of PAMAM G4 dendrimer (25 mg, 1.76 µmol) and 1,8-naphthalic anhydride (26.8 mg, 135 µmol) in DMF (1.5 mL) was stirred at 90 °C for 48 h in the dark under a nitrogen atmosphere. The crude Naph-Den product was purified by dialysis using a regenerated cellulose membrane with a molecular weight cutoff of 12–14 kDa in dimethyl sulfoxide (DMSO) for three days. The light yellow solution in the dialysis bag was dried under vacuum for four days to yield the Naph-Den as a light yellow brown semi-solid (40 mg, 85%): ^{1}H NMR (400 MHz, $CDCl_3$), δ 8.26 (br, 252H, naphthyl-H and amido-H, overlapped), 7.94 (br, 128H, naphthyl-H), 7.67 (br, 128H, naphthyl-H), 4.02 (br, 128H, CH_2 adjacent to naphthyl unit), 2.90 (s, 256H, -C*H*$_2$-CO-), 2.74 (s, 256H, -C*H*$_2$-NH-CO-), 2.09 (br, 356H, -*CH*$_2$-N-); λ_{abs} (DMSO) 330 nm. The Naph-Den-mGO slurry was prepared by vortex mixing a 6 mg mL^{-1} mGO (prepared with a modified Hummers method in which 0.5 g $KMnO_4$ for 1 g Graphite (2)) DMF suspension with a 6 mg mL^{-1} Naph-Den DMF solution.

Fabrication of Naph-Den-mGO film protected cathode

The GO-S composite material was prepared by decomposing sodium polysulfide (NaS_x) in the presence of GO (prepared with a modified Hummers method in which 4 g $KMnO_4$ used for 1 g Graphite (3)) in a water/ethanol mixed solvent. The obtained GO-S was mixed with carbon black and polyvinylidene difluoride (PVDF) in a mass ratio of 80:10:10 in *N*-methylpyrrolidone (NMP) to make a slurry that was then casted onto a carbon-coated Al foil (MTI Corporation, USA) and dried at 50 °C in a vacuum oven for 2 h. The sulfur electrode film was compressed and punched into circular pellets with a diameter of 14 mm. 20 µL of the Naph-Den-mGO slurry (6 mg mL^{-1}) was then cast onto the sulfur cathode by doctor blading, followed by drying at 50 °C in a vacuum oven for another 2 h. The BP-S electrodes were prepared by immersing BP (NTL-12214, 45 gsm MWNT Blend, Nanotech Labs, Inc.) in a 0.04 g ml^{-1} S_8/DMF solution followed by drying in a vacuum oven at 70 ^{o}C. The electrodes were then punched into circular

disks with a diameter of 14 mm. After that, the electrode disks were sealed in a Teflon lined stainless steel autoclave and heated at 155 ^{o}C for 12h. The Naph-Den-mGO/BP-S electrodes were prepared by casting the Naph-Den-mGO slurry onto the BP-S electrodes following the same procedure as for preparing the Naph-Den-mGO/GO-S electrodes.

Materials characterization

^{1}H NMR spectra were recorded with an Agilent 400 MHz NMR instrument. Chemical shifts are reported as ppm from the internal reference tetramethylsilane (TMS). Absorption spectra were recorded with a Varian Cary 50 Bio UV-visible spectrophotometer. SEM imaging and EDX measurements were performed with a Hitachi SU8230 field emission SEM microscope. TEM images were taken on a JEM-1400 Plus TEM microscope. XPS measurements were performed with a PHI Versa Probe II with Al K_{α} radiation. The XPS samples were prepared by soaking material loaded silicon chips for 24 h in a 0.01 mol L^{-1} Li_2S_4 solution prepared by dissolving stoichiometric amounts of elemental sulfur and lithium sulfide (Li_2S) in a mixed solvent of DME and DOL (1:1 by volume), followed by drying in an argon-filled glove box. The samples were then transferred into the XPS chamber without exposing to air, using an air-tight vessel.

Electrochemical measurements

CR2032 coin cells were assembled in an argon-filled glove box with the prepared sulfur electrodes as cathode, lithium disks as anode, and a porous membrane (Celgard 3501) as the separator. The electrolyte was lithium bis(trifluoromethane) sulphonimide (1.0 M) in a solvent mixture of DOL and DME (1:1 by volume) containing lithium nitrate (2 wt.%). Galvanostatic discharging and charging were performed on an Arbin BT-2143 battery analyzer at various rates (1 C = 1600 mA g^{-1}) in the potential window of 1.7-2.7 V vs Li^{+}/Li. The EIS data were recorded using a 760D electrochemistry workstation (CH Instruments) at 2.4 V over the frequency range of 100 kHz to 10 mHz. To assess the electrochemical stability of the Naph-Den-mGO film, the Naph-Den-mGO slurry was coated onto Al foil and then cut into electrode disks with a diameter of 14 mm. CR2032 coin cells were assembled using the Naph-Den-mGO electrode as cathode and Li foil as anode. CV data were recorded with the Arbin BT-2143 battery analyzer at a scan rate of 0.05 mV s^{-1}.

Computational details

The DFT study was performed with the B3LYP functional (4, 5) implemented in Gaussian 09 Rev. D.01 (6). Dispersion interactions were considered with Grimme's D3 correction (7). A pruned grid having 99 radial shells and 590 angular points per shell, called "ultrafine" grid in Gaussian 09, was used for the non-analytic integral evaluations. The 6-31G(d) basis set (8, 9) was used for the geometry optimization, Mulliken population analysis, and the vibrational frequency analysis required for free energy calculations. The calculated vibrational frequencies were used for the computation of molecular partition functions to evaluate thermal contributions to the free energy at 298.15 K by employing the ideal gas, rigid rotator, harmonic oscillator approximation (10). The 6-311+G(2df,p) basis set (11) was used in single-point calculations for refined energetics. The thermal contribution to the free energies from the frequency analysis was added to the refined energetics for all final composite free energies reported in the manuscript. In the calculation of binding free energies, the 1 M standard state was used for all species.

SUPPORTING FIGURES

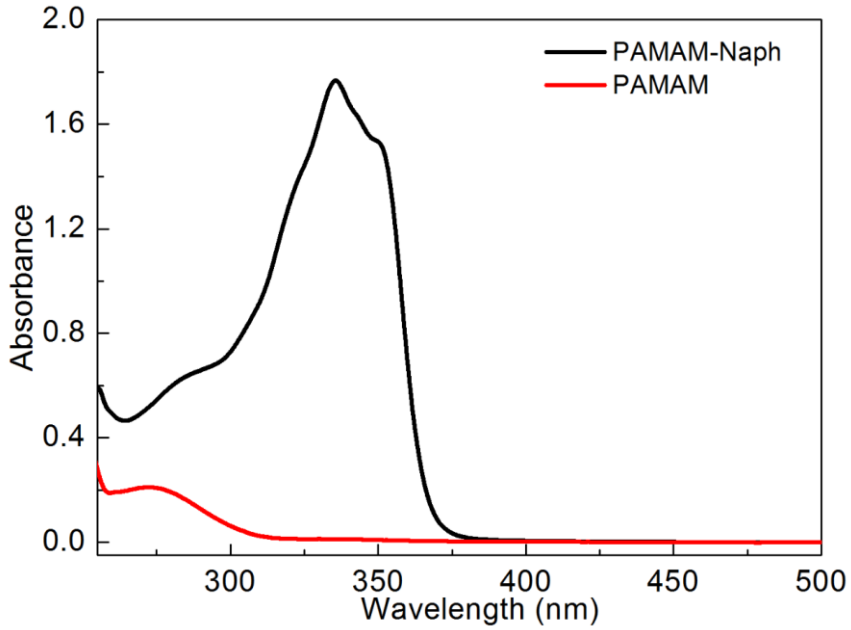

Figure S1 UV-Vis absorption spectra. Both the dendrimer (PAMAM) and its naphthalimide functionalized product Den-Naph (PAMAM-Naph) were measured in DMSO at a concentration of 0.5 mg mL^{-1}.

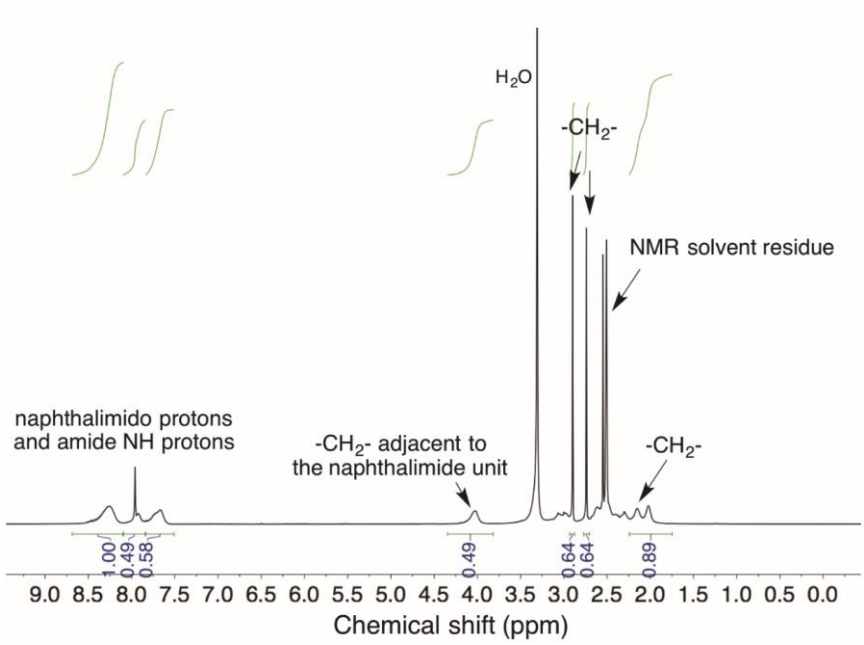

Figure S2 ^{1}H NMR spectrum of Den-Naph in DMSO-d6.

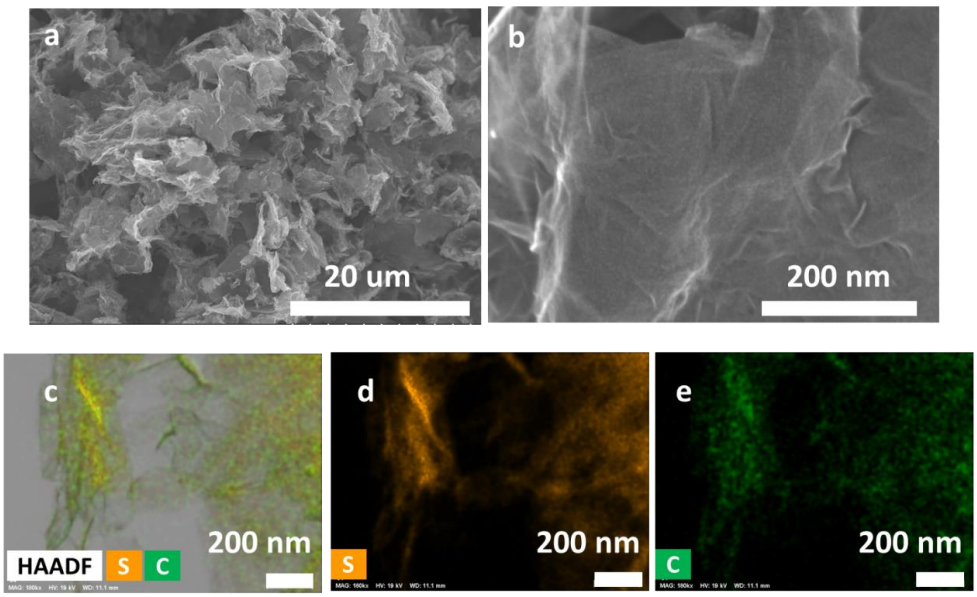

Figure S3 Morphology and elemental distribution of GO-S cathode material with 65 wt.% sulfur content. SEM images of GO-S at low (a) and high (b) magnification. (c, d, e) HAADF image and EDX maps of GO-S.

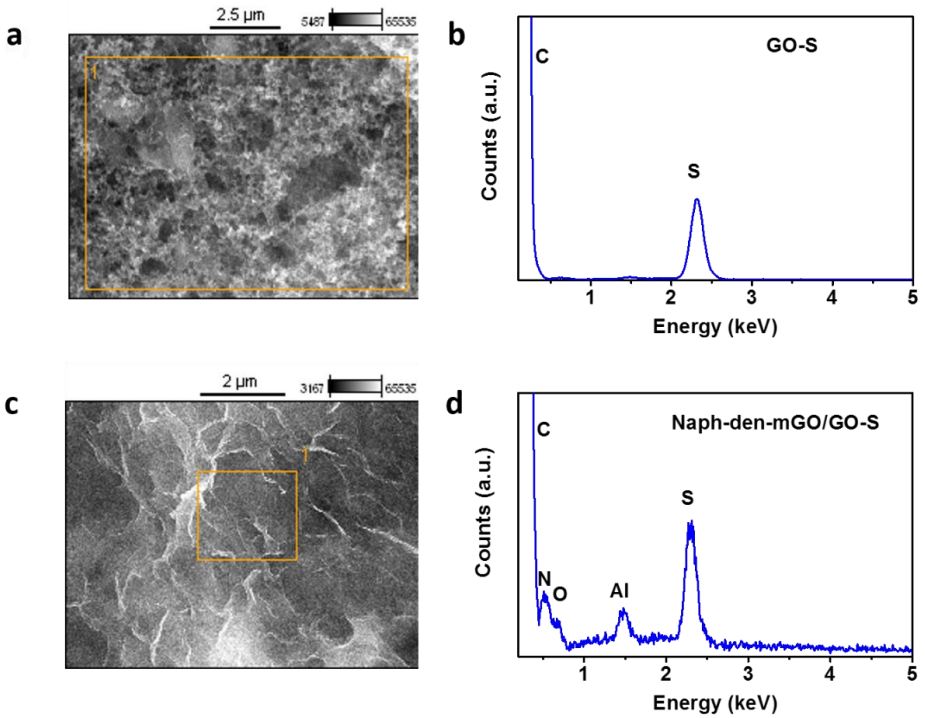

Figure S4 SEM and EDX analysis for sulfur electrodes. (a, b) SEM image and corresponding EDX spectrum of the GO-S electrode. (c, d) SEM image and corresponding EDX spectrum of the Naph-Den-mGO/GO-S electrode.

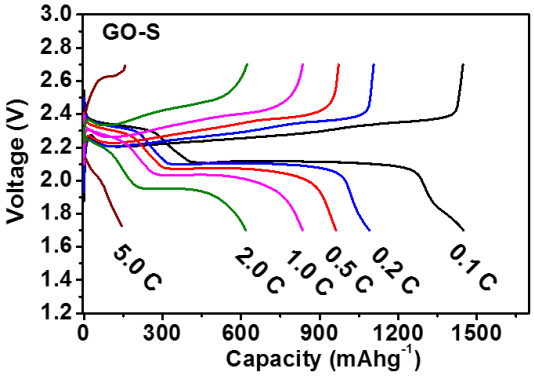

Figure S5 Representative discharging-charging voltage profiles of GO-S at different C rates.

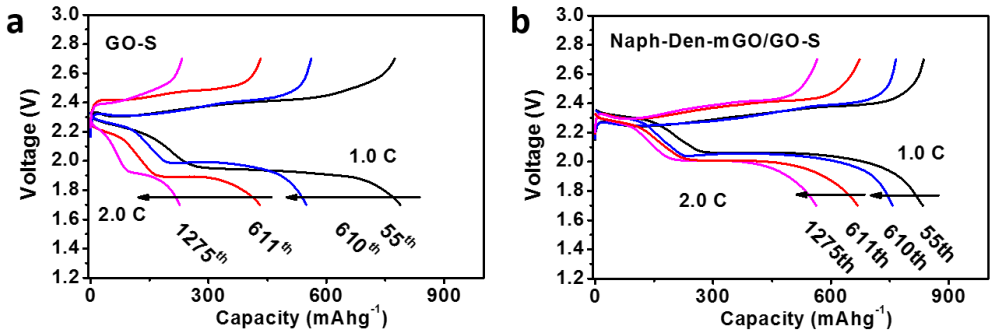

Figure S6 Discharging and charging voltage profiles of the GO-S electrodes with and without the Naph-Den-mGO film at different stages of cycling stability test. The sulfur content in the GO-S composite is 65 wt.%, and the total sulfur loading on the electrode is 1 mg cm^{-2}.

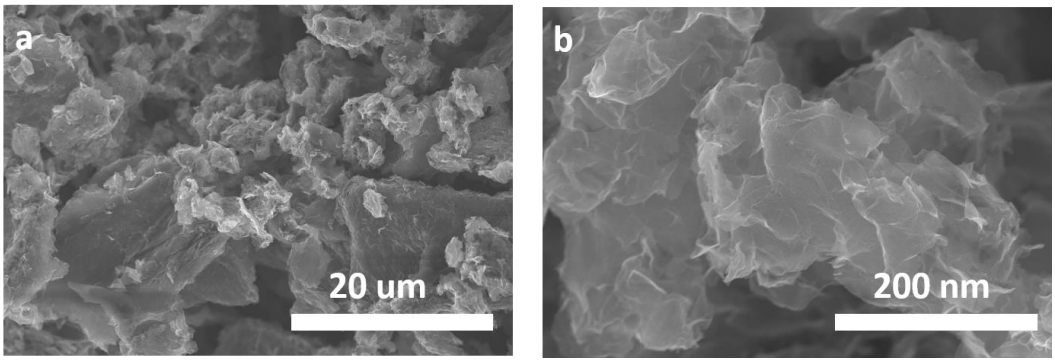

Figure S7 Morphology of the GO-S cathode material with 76 wt.% sulfur content. SEM images of the GO-S at low (a) and high (b) magnification.

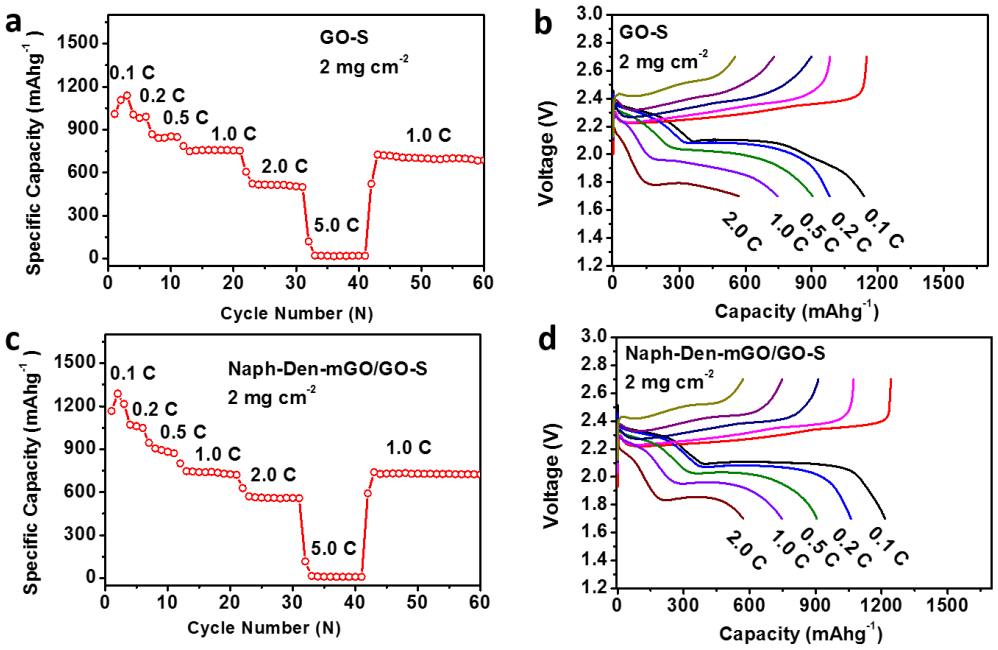

Figure S8 Electrochemical performance of the Naph-Den-mGO/GO-S electrode compared with the GO-S electrode. (a) Discharge capacities and (b) representative discharging-charging voltage profiles of the GO-S electrode at different C rates. (c) Discharge capacities and (d) representative discharging-charging voltage profiles of the Naph-Den-mGO/GO-S electrode at different C rates. The sulfur content in the GO-S composite is 76 wt.%, and the sulfur mass loading on the electrode is 2 mg cm^{-2}.

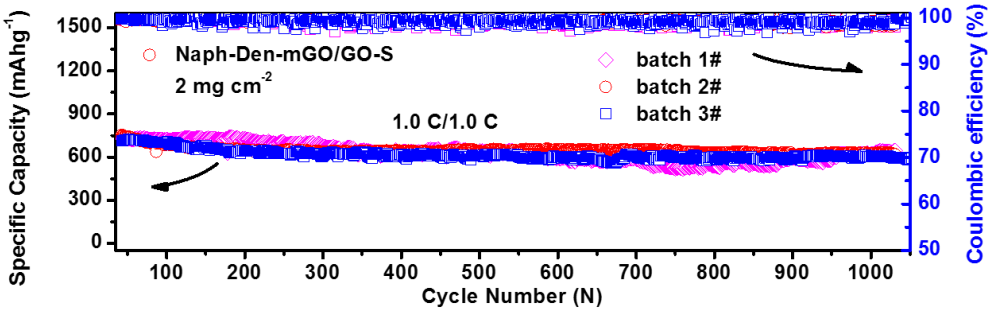

Figure S9 Parallel cycling stability test of the Naph-Den-mGO/GO-S electrodes. The sulfur content in the GO-S composite is 76 wt.%, and the sulfur mass loading on the electrode is 2 mg cm^{-2}.

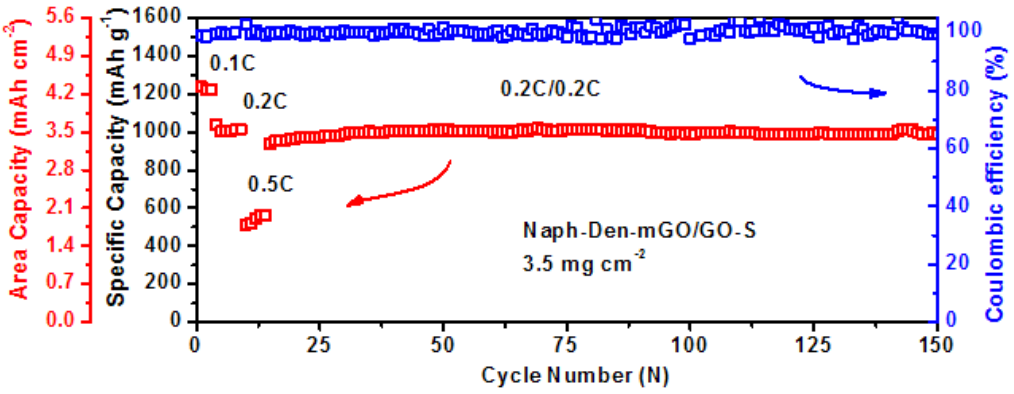

Figure S10 Cycling performance of Naph-Den-mGO/GO-S electrode at 0.2 C. The sulfur content in the GO-S composite is 76 wt.%, and the sulfur mass loading on the electrode is 3.5 mg cm^{-2}.

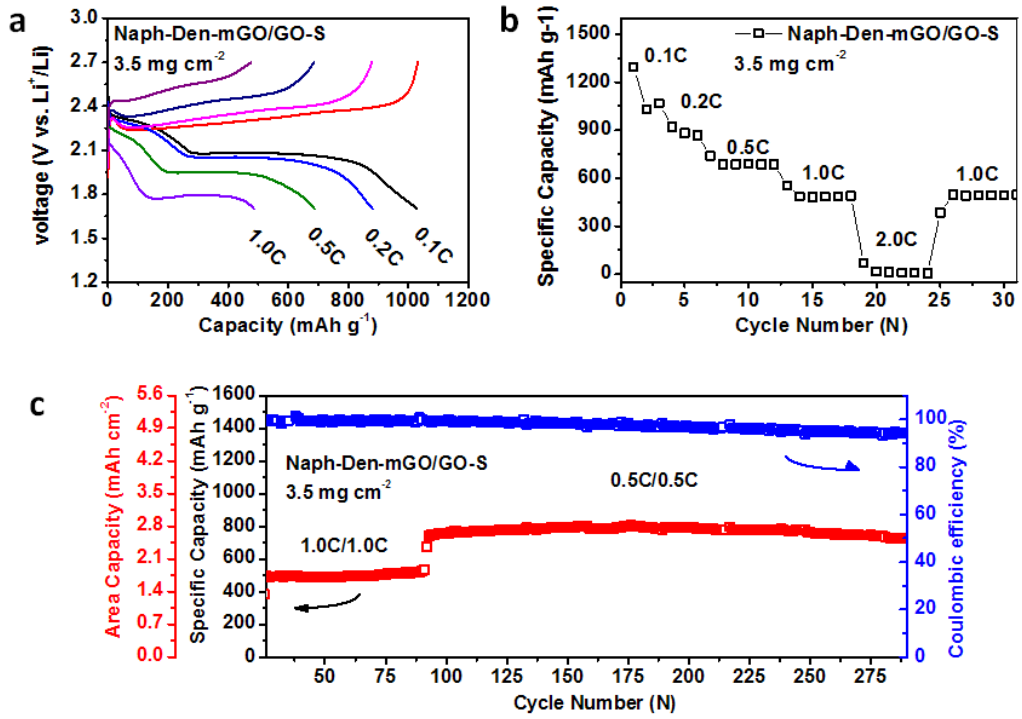

Figure S11 Electrochemical performance of the Naph-Den-mGO/GO-S electrode with high sulfur mass loading. (a) Representative discharging-charging voltage profiles. (b) Discharging capacities at different C rates. (c) Cycling stability at 1.0 C and 0.5 C. The sulfur content in the GO-S composite is 76 wt.%, and the sulfur mass loading on the electrode is 3.5 mg cm^{-2}.

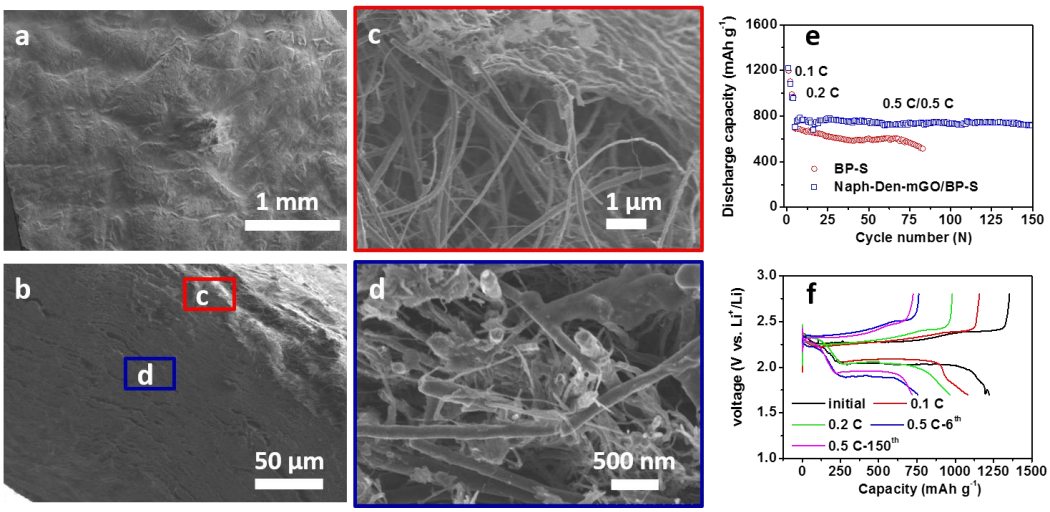

Figure S12 SEM images and electrochemical performance of the Naph-Den-mGO/BP-S electrode. (a) Top-view and (b) cross-section SEM images of the Naph-Den-mGO/BP-S electrode. (c) Enlarged cross-section SEM image showing the Naph-Den-mGO film on the electrode surface. (d) Enlarged cross-section SEM image showing the carbon nanotubes coated with sulfur particles. (e) Cycling stability of the BP-S and Naph-Den-mGO/BP-S electrodes. (f) Discharging-charging voltage profiles of the Naph-Den-mGO/BP-S electrode.

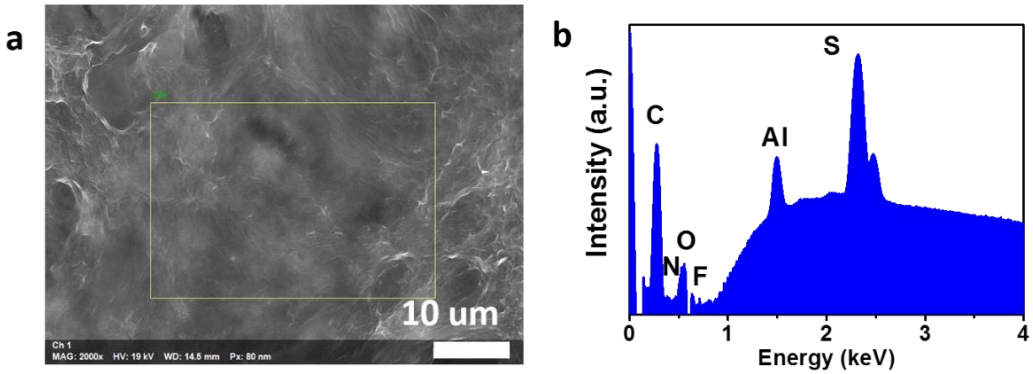

Figure S13 SEM and EDX characterization of the Naph-Den-mGO/GO-S electrode after cycling (1275 cycles).

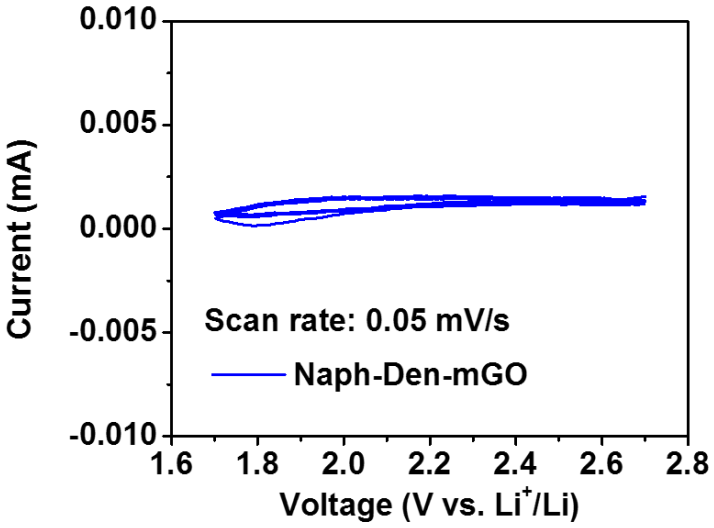

Figure S14 Cyclic voltammograms of the Naph-Den-mGO film in the Li-S battery electrolyte

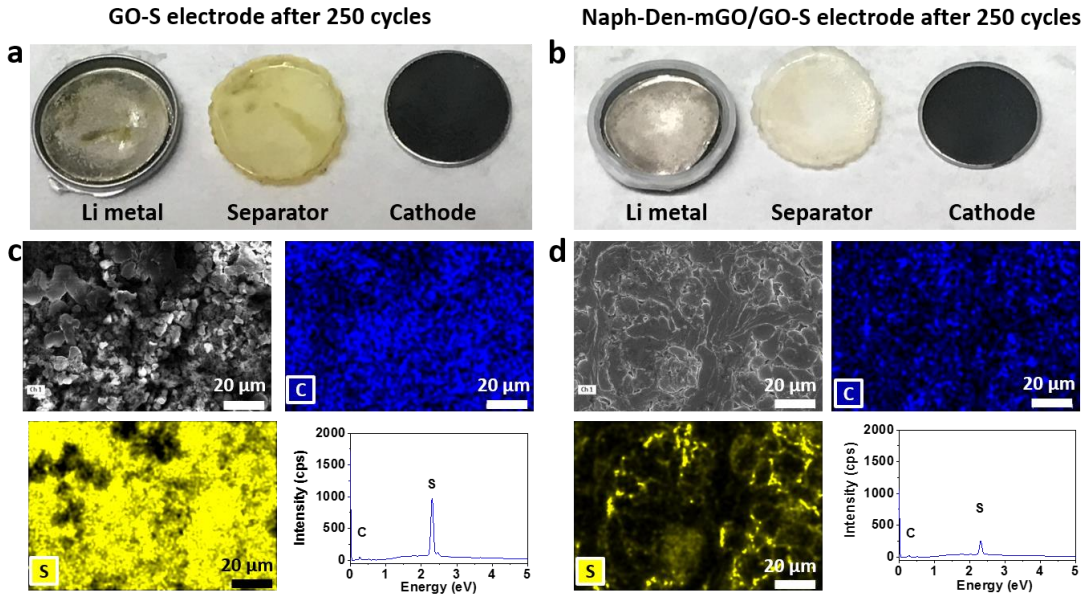

Figure S15. Postmortem analysis of the Li anodes paired with the GO-S and Naph-Den-mGO/GO-S cathodes in cells after 250 cycles. Photographs of the disassembled cells using (a) GO-S and (b) Naph-Den-mGO/GO-S as cathodes. SEM images and the corresponding EDS spectra and elemental maps of the cycled Li anodes paired with the (c) GO-S and (d) Naph-Den-mGO/GO-S cathodes.

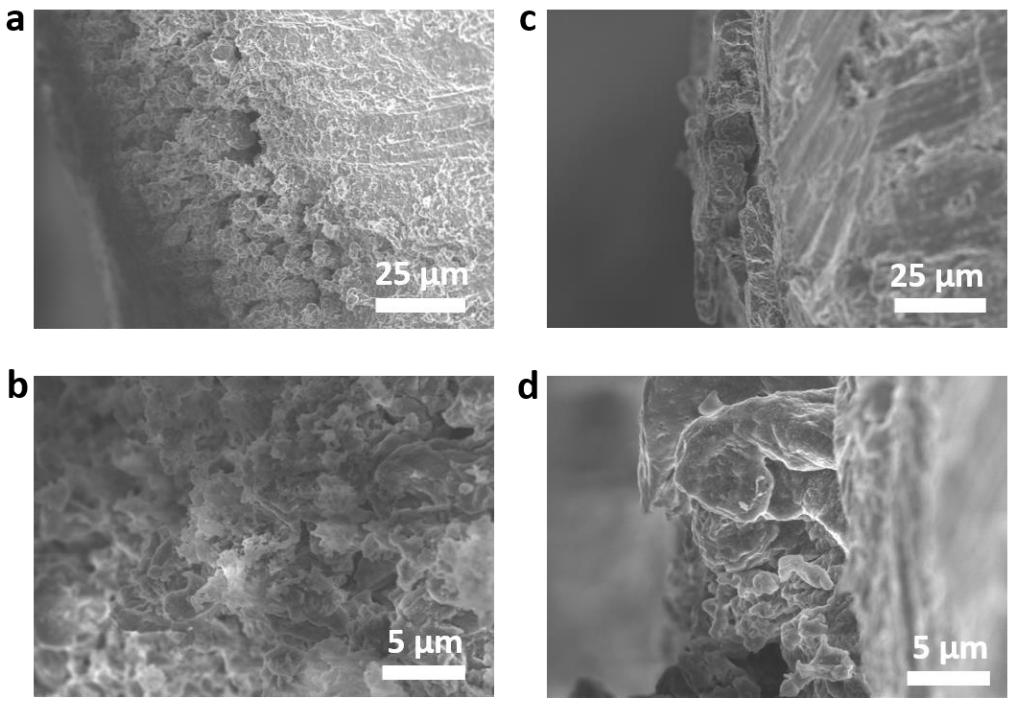

Figure S16. Cross-section SEM images of the Li anodes paired with the (a, b) GO-S and (c, d) Naph-Den-mGO/GO-S cathodes after 250 cycles.

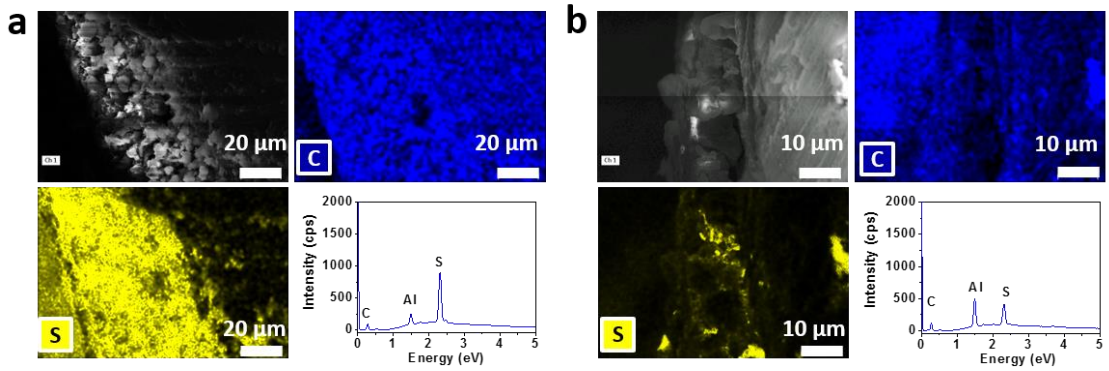

Figure S17. SEM-EDS analysis of the cross sections of the Li anodes paired with the (a) GO-S and (b) Naph-Den-mGO/GO-S cathodes after 250 cycles.

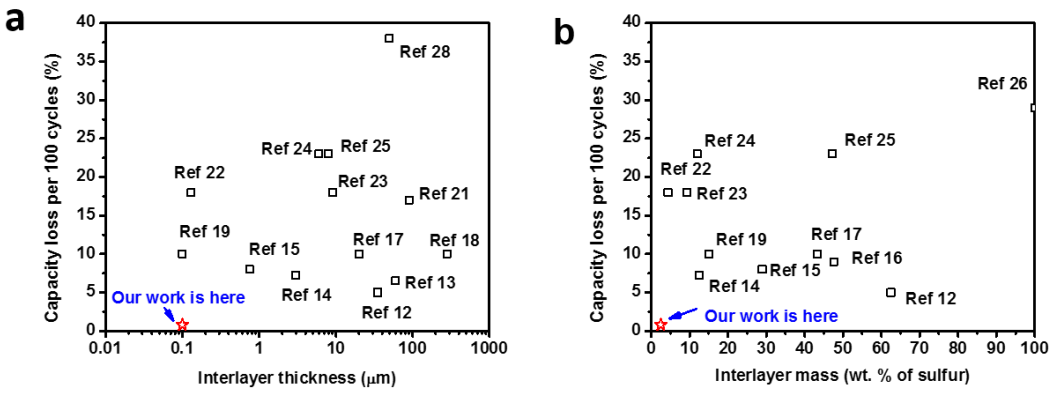

Figure S18 Figures of merit for Li-S battery cathode interlayers reported in the literature (Table S1). (a) Plot of cathode capacity loss upon cycling against interlayer thickness. (b) Plot of cathode capacity loss upon cycling against interlayer mass (percentage of sulfur active material). Our Naph-Den-mGO film outperforms any other interlayer reported to date.

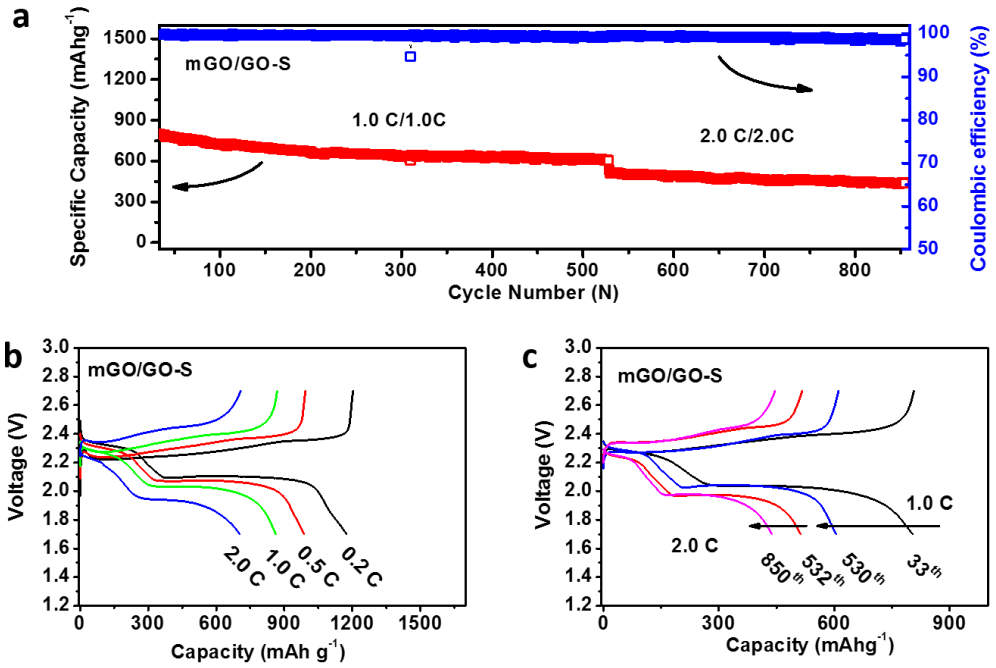

Figure S19 Electrochemical performance of the mGO/GO-S electrode. (a) Cycling stability at 1.0 and 2.0 C rates. (b) Representative discharging-charging voltage profiles at different C rates. (c) The discharging-charging voltage profiles before and after cycling at 1.0 and 2.0 C. The sulfur content in the GO-S composite is 65 wt.%, and the total sulfur loading on the electrode is 1 mg cm^{-2}.

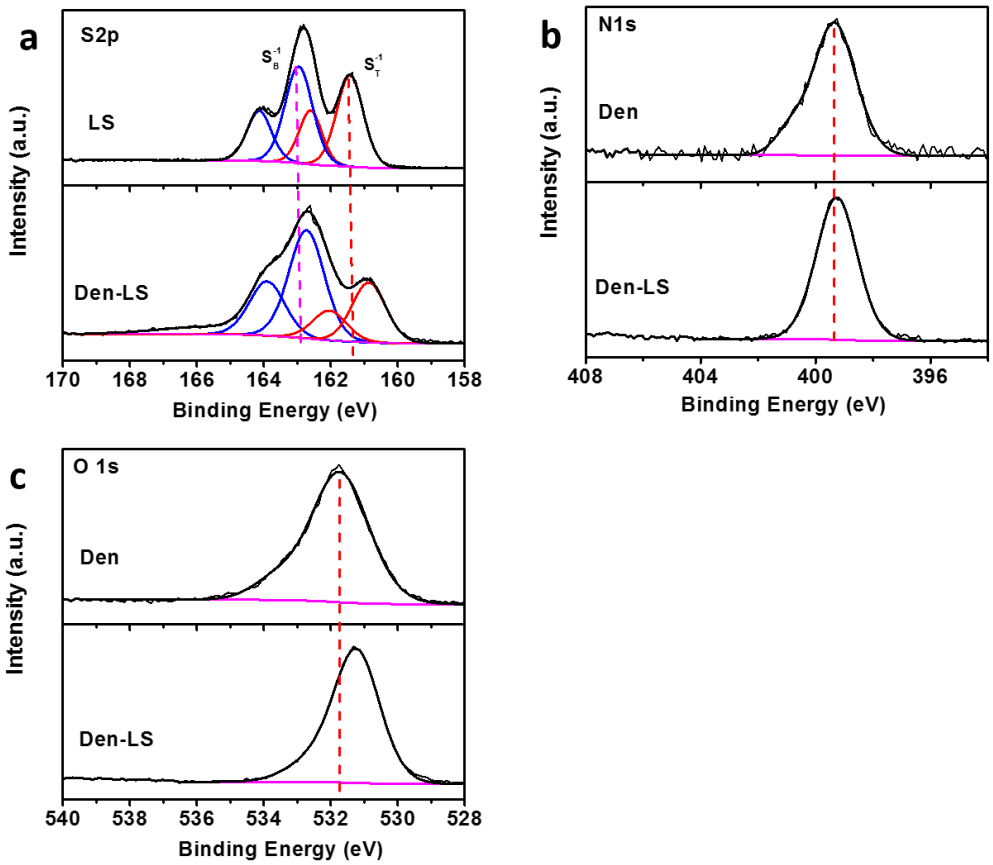

Figure S20 XPS analysis of the interaction between lithium polysulfide and the unmodified dendrimer (PAMAM). (a) S 2p core level spectra of free Li_2S_4 and Li_2S_4 adsorbed on PAMAM. (b) N 1s and (c) O 1s core level spectra of the PAMAM before and after its interaction with Li_2S_4.

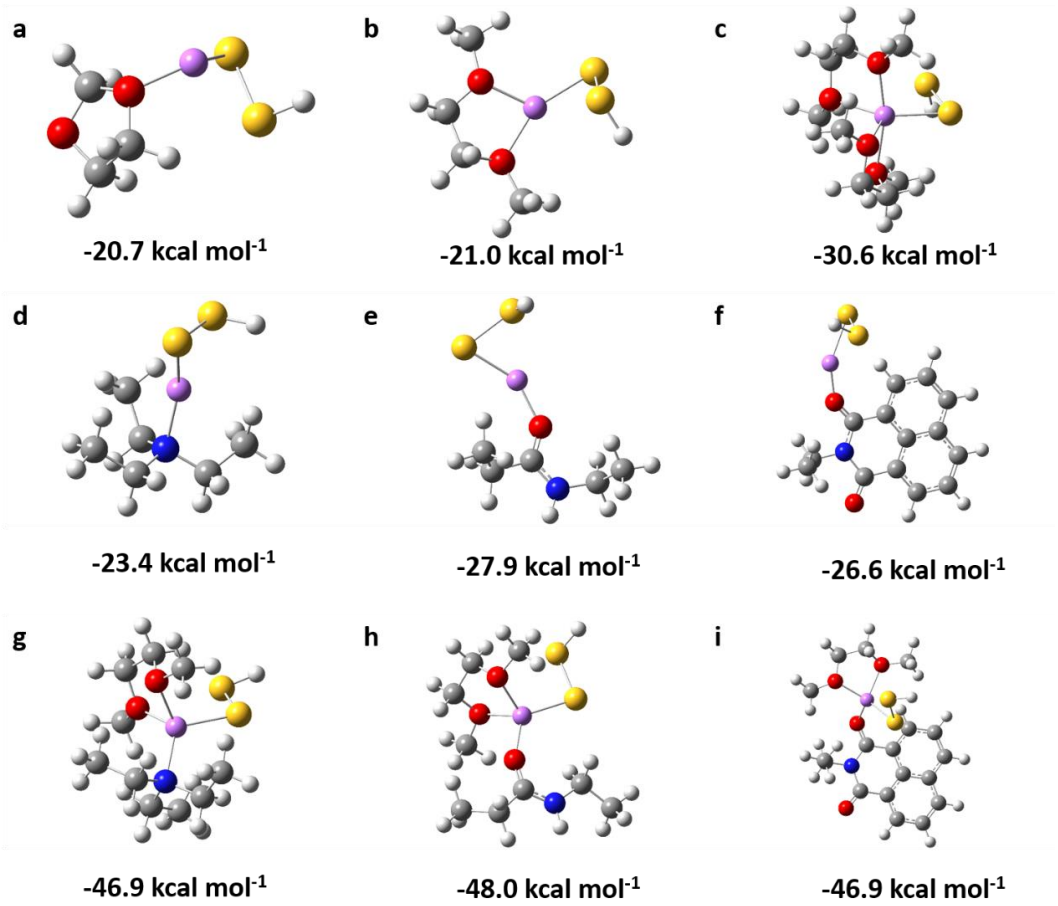

Figure S21 Theoretical calculations of binding energy (ΔE_B). Optimized geometries for the binding of LiSSH to (**a**) DOL, (**b**) DME, (**c**) two DME molecules, (**d**) N1 site, (**e**) O1 site, (**f**) Ot site, (**g**) N1 site and one DME molecule, (**h**) O1 site and one DME molecule, and (**i**) Ot site and one DME molecule, together with the corresponding binding energies in kcal/mol. Grey, white, red, blue, yellow, and purple balls represent C, H, O, N, S, and Li atoms, respectively.

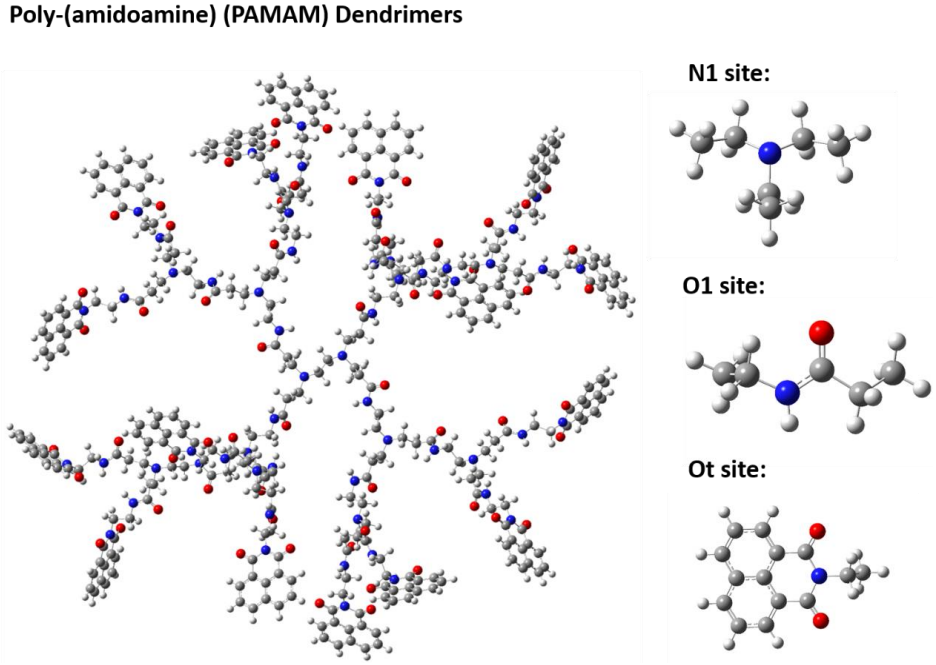

Figure S22 Structure of the PAMAM G2 dendrimer and three possible binding sites for lithium polysulfides. Grey, white, red, and blue balls represent C, H, O, and N atoms, respectively.

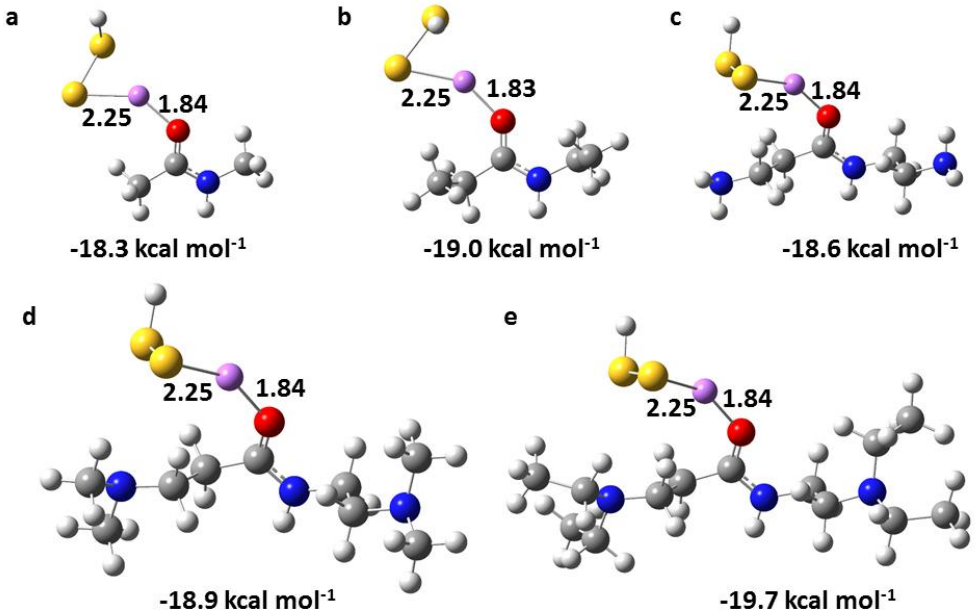

Figure S23 Optimized geometries for the binding of LiSSH to the O1 sites. Models include (**a**) 1 bond, (**b**) 2 bonds, (**c**) 3 bonds, (**d**) 4 bonds, and (**e**) 5 bonds beyond the amide group. The calculated binding free energies and key bond lengths are shown in kcal/mol and Å. Grey, white, red, blue, yellow, and purple balls represent C, H, O, N, S, and Li atoms, respectively.

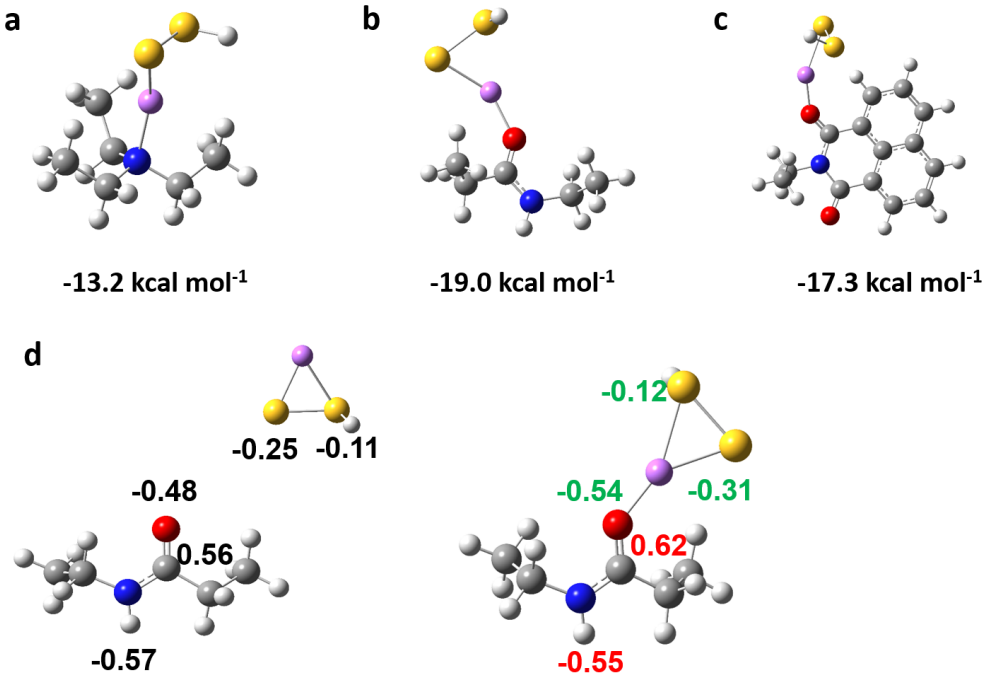

Figure S24 Theoretical calculations in the absence of solvent molecules. Optimized geometries for the binding of LiSSH to (a) N1 site, (b) O1 site, and (c) Ot site of Naph-Den, with the binding free energies in kcal mol^{-1}; Mulliken charges (d) before and (e) after LiSSH binding to the O1 site of Naph-Den. Grey, white, red, blue, yellow, and purple balls represent C, H, O, N, S, and Li atoms, respectively.

SUPPORTING TABLES

Table S1. Performance comparison with sulfur cathodes protected by different interlayers reported in the literature (green: average capacity decay <2% per 100 cycles; yellow: 2-10%; red: >10%).

Interlayer	Sulfur loading ($mg\ cm^{-2}$)	Interlayer thickness (μm)	Interlayer mass ($mg\ cm^{-2}$)	Cycling stability		Ref.
				Cycles	Capacity loss per 100 cycles	
Naph-Den-mGO	**2.0**	**0.1**	**~0.05**	**500**	**0.8%@1 C**	**This work**
TiO_2-CNT	0.8	35	0.5~0.6	500	5%@1 C	(12)
Carbon/MWCNT paper	1.8~2.7	~60	\	100	6.5%@1 C	(13)
GO-TiO_2	1.2	~3	0.15	250	7.2%@0.5 C	(14)
GO	1~1.2	0.75	0.29	400	8%@1 C	(15)
N,P co-doped graphene	2.1	\	1.0	500	9%@1 C	(16)
Graphene	3~4	20	1.3	300	10%@1 C	(17)
Carbon nanofibers	1.4	~280	4.2	100	10%@1 C	(18)
Ethylenediamine-functionalized rGO	3.6	0.1	0.54	200	10%@0.2 C	(19)
Microporous carbon paper	\	\	\	100	15%@1 C	(20)
Ni foam	\	~90	\	50	17%@0.2 C	(21)
GO/Nafion	1.2	0.13	0.0532	200	18%@0.5 C	(22)
SWCNT	1.5	~9	0.14	300	18%@0.2 C	(23)
GO	1~1.5	~6	0.12	100	23%@0.1 C	(24)
N doped graphene paper	1.06	~8	0.5	100	23%@0.2 C	(25)
rGO-carbon black	3	\	3	100	29%@0.2 C	(26)
Al_2O_3-activated carbon cloth	12	500	~2	40	\	(27)
MWCNT	\	40~50	0.6~0.8	100	38%@1 C	(28)

Table S2. Performance comparison with state-of-the-art high-performance sulfur cathodes reported in the literature (green: average capacity decay <2% per 100 cycles; yellow: 2-10%; red: >10%).

Cathode	Sulfur content in material	Sulfur loading on electrode (mg cm^{-2})	Cycling stability			Ref.
			Capacity (mAh g^{-1})	Cycles	Loss per 100 cycles	
Naph-Den-mGO/GO-S	**65%**	**1.0**	**830**	**560**	**1.6%@1 C**	**This work**
	76%	**2.0**	**727**	**1000**	**1%@1 C**	
	76%	**3.5**	**741**	**200**	**1.1%@0.5 C**	
Covalent bond glued sulfur nanosheets	83%	1.2	715	500	2.1%@0.625C	(29)
S-TiO_2 yolk-shell	71%	0.4-0.6	1030	1000	3.3%@0.5C	(30)
CoS_2-graphene/S	75%	0.4	1000	2000	3.4%@2C	(31)
MnO_2 nanosheets/S	75%	0.7-1.0	870	2000	3.6%@2C	(32)
Mesoporous carbon sphere-CNT/S	70%	5	1200	200	5%@0.2C	(33)
Hollow carbon nanospheres/S	67%	\	842	500	5.3%@1C	(34)
Si/SiO_2@C-S	70%	3.1-3.5	890	500	6.3%@2C	(35)
Ti_4O_7/S	60%	1.5-1.8	850	500	6%@2C	(36)
ethylenediamine-functionalized rGO/S	69%	/	700	350	7%@0.5C	(37)
S/Co-N-Graphitic carbon	70%	2.5	795	500	9%@1C	(38)
Graphene-S sandwich	70%	3~4	1000	300	10%@1C	(17)
Dual confined N-doped double-shelled hollow carbon spheres/S	63%	3.9	838	200	19%@0.5C	(39)

SUPPORTING REFERENCES

1. Kauffman DR, Shade CM, Uh H, Petoud S, Star A (2009) Decorated carbon nanotubes with unique oxygen sensitivity. *Nat Chem* 1(6):500-506.
2. Liang Y*, et al.* (2011) Co3O4 nanocrystals on graphene as a synergistic catalyst for oxygen reduction reaction. *Nat Mater* 10(10):780-786.
3. Liu W*, et al.* (2016) A highly active and stable hydrogen evolution catalyst based on pyrite-structured cobalt phosphosulfide. *Nat Commun* 7:10771.
4. Becke AD (1993) Density-functional thermochemistry. III. The role of exact exchange. *J Chem Phys* 98(7):5648-5652.
5. Stephens PJ, Devlin FJ, Chabalowski CF, Frisch MJ (1994) Ab Initio Calculation of Vibrational Absorption and Circular Dichroism Spectra Using Density Functional Force Fields. *J Phys Chem* 98(45):11623-11627.
6. Frisch MJ*, et al.* (2009) Gaussian 09 (Gaussian, Inc., Wallingford, CT), Rev. D.01.
7. Grimme S, Antony J, Ehrlich S, Krieg H (2010) A consistent and accurate ab initio parametrization of density functional dispersion correction (DFT-D) for the 94 elements H-Pu. *J Chem Phys* 132(15):154104.
8. Hariharan PC, Pople JA (1973) The influence of polarization functions on molecular orbital hydrogenation energies. *Theoret Chim Acta* 28(3):213-222.
9. Francl MM*, et al.* (1982) Self-consistent molecular orbital methods. XXIII. A polarization-type basis set for second-row elements. *J Chem Phys* 77(7):3654-3665.
10. Cramer CJ (2004) *Essentials of Computational Chemistry: Theories and Models* (Wiley, Chichester, U. K.) 2nd ed.
11. Frisch MJ, Pople JA, Binkley JS (1984) Self-consistent molecular orbital methods 25. Supplementary functions for Gaussian basis sets. *J Chem Phys* 80(7):3265-3269.
12. Liang G*, et al.* (2016) Ultrafine TiO_2 Decorated Carbon Nanofibers as Multifunctional Interlayer for High-Performance Lithium–Sulfur Battery. *ACS Appl Mater* 8(35):23105-23113.
13. Hwang JY*, et al.* (2016) High-Energy, High-Rate, Lithium-Sulfur Batteries: Synergetic Effect of Hollow TiO_2-Webbed Carbon Nanotubes and a Dual Functional Carbon-Paper Interlayer. *Adv Energy Mater* 6(1):1501480.
14. Xiao Z*, et al.* (2015) A Lightweight TiO_2/Graphene Interlayer, Applied as a Highly Effective Polysulfide Absorbent for Fast, Long-Life Lithium–Sulfur Batteries. *Adv Mater* 27(18):2891-2898.
15. Shaibani M*, et al.* (2016) Suppressed Polysulfide Crossover in Li–S Batteries through a High-Flux Graphene Oxide Membrane Supported on a Sulfur Cathode. *ACS Nano* 10(8):7768-7779.
16. Gu X*, et al.* (2015) A porous nitrogen and phosphorous dual doped graphene blocking layer for high performance Li-S batteries. *J Mater Chem A* 3(32):16670-16678.
17. Zhou G*, et al.* (2014) A Graphene–Pure-Sulfur Sandwich Structure for Ultrafast, Long-Life Lithium–Sulfur Batteries. *Adv Mater* 26(4):625-631.
18. Singhal R, Chung SH, Manthiram A, Kalra V (2015) A free-standing carbon nanofiber interlayer for high-performance lithium-sulfur batteries. *J Mater Chem A* 3(8):4530-4538.

19. Li Z, Zhang JT, Chen YM, Li J, Lou XW (2015) Pie-like electrode design for high-energy density lithium-sulfur batteries. *Nat Commun* 6:8850.
20. Su YS, Manthiram A (2012) Lithium–sulphur batteries with a microporous carbon paper as a bifunctional interlayer. *Nat Commun* 3:1166.
21. Zhang K*, et al.* (2014) Nickel foam as interlayer to improve the performance of lithium–sulfur battery. *J Solid State Electr* 18(4):1025-1029.
22. Zhuang TZ*, et al.* (2016) Rational Integration of Polypropylene/Graphene Oxide/Nafion as Ternary-Layered Separator to Retard the Shuttle of Polysulfides for Lithium–Sulfur Batteries. *Small* 12(3):381-389.
23. Chang CH, Chung SH, Manthiram A (2016) Effective Stabilization of a High-Loading Sulfur Cathode and a Lithium-Metal Anode in Li-S Batteries Utilizing SWCNT-Modulated Separators. *Small* 12(2):174-179.
24. Huang JQ*, et al.* (2015) Permselective Graphene Oxide Membrane for Highly Stable and Anti-Self-Discharge Lithium–Sulfur Batteries. *ACS Nano* 9(3):3002-3011.
25. Han K*, et al.* (2014) Free-Standing Nitrogen-doped Graphene Paper as Electrodes for High-Performance Lithium/Dissolved Polysulfide Batteries. *ChemSusChem* 7(9):2545-2553.
26. Wang X, Wang Z, Chen L (2013) Reduced graphene oxide film as a shuttle-inhibiting interlayer in a lithium–sulfur battery. *J Power Sources* 242:65-69.
27. Han X*, et al.* (2013) Reactivation of dissolved polysulfides in Li–S batteries based on atomic layer deposition of Al_2O_3 in nanoporous carbon cloth. *Nano Energy* 2(6):1197-1206.
28. Su YS, Manthiram A (2012) A new approach to improve cycle performance of rechargeable lithium–sulfur batteries by inserting a free-standing MWCNT interlayer. *Chem Commun* 48(70):8817-8819.
29. Wang L, Dong Z, Wang D, Zhang F, Jin J (2013) Covalent Bond Glued Sulfur Nanosheet-Based Cathode Integration for Long-Cycle-Life Li–S Batteries. *Nano Lett* 13(12):6244-6250.
30. Wei Seh Z*, et al.* (2013) Sulphur–TiO_2 yolk–shell nanoarchitecture with internal void space for long-cycle lithium–sulphur batteries. *Nat Commun* 4:1331.
31. Yuan Z*, et al.* (2016) Powering Lithium–Sulfur Battery Performance by Propelling Polysulfide Redox at Sulfiphilic Hosts. *Nano Lett* 16(1):519-527.
32. Liang X*, et al.* (2015) A highly efficient polysulfide mediator for lithium-sulfur batteries. *Nat Commun* 6:5682.
33. Song J*, et al.* (2015) Strong Lithium Polysulfide Chemisorption on Electroactive Sites of Nitrogen-Doped Carbon Composites For High-Performance Lithium–Sulfur Battery Cathodes. *Ang Chem Int Ed* 127(14):4399-4403.
34. Xu F*, et al.* (2015) Facile synthesis of ultrahigh-surface-area hollow carbon nanospheres for enhanced adsorption and energy storage. *Nat Commun* 6:7221.
35. Rehman S, Guo S, Hou Y (2016) Rational Design of Si/SiO_2@Hierarchical Porous Carbon Spheres as Efficient Polysulfide Reservoirs for High-Performance Li–S Battery. *Adv Mater* 28(16):3167-3172.
36. Pang Q, Kundu D, Cuisinier M, Nazar LF (2014) Surface-enhanced redox chemistry of polysulphides on a metallic and polar host for lithium-sulphur batteries. *Nat Commun* 5:4759.

37. Wang Z*, et al.* (2014) Enhancing lithium–sulphur battery performance by strongly binding the discharge products on amino-functionalized reduced graphene oxide. *Nat Commun* 5:5002.
38. Li YJ, Fan JM, Zheng MS, Dong QF (2016) A novel synergistic composite with multi-functional effects for high-performance Li-S batteries. *Energy Environ Sci* 9(6):1998-2004.
39. Zhou G, Zhao Y, Manthiram A (2015) Dual-Confined Flexible Sulfur Cathodes Encapsulated in Nitrogen-Doped Double-Shelled Hollow Carbon Spheres and Wrapped with Graphene for Li-S Batteries. *Adv Energy Mater* 5(9):1402263.